1 **Spatial transcriptomic analysis of HIV and tuberculosis coinfection in a humanized mouse**

2 **model reveals specific transcription patterns, immune responses and early morphological**

3 **alteration signaling**

4 Sitaramaraju Adduri[1#], Jose Alejandro Bohorquez[1#], Omoyeni Adejare[1], Diego Rincon[2], Torry

5 Tucker[1], Nagarjun V Konduru[1], Guohua Yi[1*]

6   1. Department of Cellular and Molecular Biology, School of Medicine, The University of

7   Texas Health Science Center at Tyler, 11937 US HWY 271, Tyler, TX 75708, USA

8   2. Unaffiliated pathologist

9 *Corresponding author: Guohua.yi@uttyler.edu

10 #Authors contributed equally to this work

11

12   **Abstract**

13   *Mycobacterium tuberculosis* (*Mtb*) and human immunodeficiency virus (HIV) coinfection is one

14   of the biggest public health concerns worldwide. Both pathogens are adept at modulating immune

15   response and, in the case of *Mtb*, even inducing structural modification of the affected tissue. The

16   present study aimed at understanding the early phenotypical and functional changes in immune

17   cell infiltration in the affected organ, using a humanized mouse model. The humanized mice were

18   infected with either HIV or *Mtb* in single infection, or with both pathogens in coinfection. Three

19   weeks after the infection, lung samples were collected, and spatial transcriptomics analysis was

20   performed. This analysis revealed high infiltration of $CD4^+$ T cells in *Mtb* infection, but not in HIV

21   or coinfection. Coinfected mice also showed a minimal number of NK cells compared to the other

22   groups. In addition to infection status, histological features also influenced the immune cell

23   infiltration pattern in the lungs. Two distinct airway regions with distinct immune cell abundance

24   patterns were detected by spatial transcriptome profiling. A lymphoid cell aggregate detected in

25   coinfection lung exhibited distinct transcript profile. The cellular architecture in the lymphoid cell

26   aggregate did not follow the spatial patterns seen in mature granulomas. However, lymphoid cell

27   aggregates exhibited granuloma gene expression signatures, and pathways associated with reactive

28   oxygen species production, oxidative phosphorylation, and TGFβ and interferon signaling similar

29   to granulomas. This study revealed specific transcription patterns, immune responses and

30   morphological alteration signaling in the early stage of HIV and *Mtb* infections.

31

Introduction

32

33   Tuberculosis (TB), caused by *Mycobacterium tuberculosis* (*Mtb*), continues to be a major

34   public health concern. It has been estimated that as much as 25% of the world population is infected

35   with *Mtb*, although most of these cases will develop the latent form of TB (LTBI)[1]. One of the

36   main features of *Mtb* is its ability to modulate immune response to generate the latent disease form.

37   This immune modulation takes place in circulating immune cells, but also extends to tissue resident

38   cells, where *Mtb* is able to induce structural modification of the hosts tissue to create specialized

39   histological structures called granulomas[2,3]. These structures are composed of a necrotic core,

40   surrounded by different immune cell populations that contain the pathogen, preventing its spread

41   throughout the host and the development of active TB. Consequently, increasing interest has been

42   granted to the cellular infiltration in lung tissue during *Mtb* infection, in general, and in

43   granulomas, in particular[4-6]. The modification of cellular subsets in the affected organ and the inter-

44   cellular communication taking place provides an explanation for how they favor or deter pathogen

45   dissemination. It has been posed that there are multiple microenvironments present within

46   granuloma structures that induce an immunoregulatory environment with differential signaling, as

47   determined by pathway activation and cytokine production, playing a crucial role in the

48   maintenance of the structure[7].

49   Accordingly, local or generalized immune alterations can lead to changes in the granuloma

50   structures that can facilitate bacterial growth[8,9]. The Human immunodeficiency virus (HIV) is one

51   of the most important disruptors of the immune response and causes instability in the granuloma

52   structures[9]. Coinfection with HIV in *Mtb*-infected individuals severely increases the probability of

53   developing active TB[10], due to the generalized immunosuppression caused by the depletion of

54   CD4+ T cells, the main target for HIV infection, as well as the specific depletion of this cell subset

55   in the granulomas. Reports show that CD4^{+} populations within granulomas are particularly

56   susceptible to HIV infection, due to increased expression of the CCR5 coreceptor[8]. Additionally,

57   given the importance of CD4^{+} cells for CD8^{+} cell maturation, HIV-induced CD4^{+} cell depletion

58   reduces the circulating effector and memory CD8^{+} cells and promotes immunosenescence in these

59   cells, rendering them dysfunctional[11].

60   Studies dedicated to understanding the cellular composition and intercellular networks

61   present locally in lung during *Mtb* infection and HIV/*Mtb* coinfection have focused on infection

62   models or samples in which the infections and structural changes are already set in the host, leaving

63   a gap in the knowledge of the early events taking place after infection[5-8,12]. This is partially due to

64   the use of stored human samples or non-human primate (NHP) animal models for these

65   experiments, which, though highly reliable, limit the availability of samples from early infection

66   timepoints. Recent reports show the feasibility of humanized mice as a model for the study of *Mtb*

67   and HIV[13,14]. These models are able to reproduce immune changes caused by infection, including

68   formation of lung granulomas. Given this, the aim of the present study was to evaluate the changes

69   in the cellular repertoire in the lung induced by HIV and *Mtb* in single infections, as well as in

70   coinfection, at an early timepoint in which granulomas have not been fully established.

71   Furthermore, we analyzed the transcriptomic changes in these cells, using a spatial approach, to

72   determine alterations in cytokine production in the affected areas. This allowed us to assess the

73   molecular processes taking place during infection, including evidence of changes in early

74   granuloma formation.

75   **Materials and methods**

76   **Generation of humanized mice**

77   Mice from the NOD.Cg-Prkdcscid Il2rgtm1Wjl Tg(CMV-IL3,CSF2,KITLG)1Eav

78   Tg(IL15)1Sz/J (NSG-SGM3-IL15) strain (The Jackson laboratory, Bar Harbor, ME), maintained

79   at the animal housing facility in the University of Texas Health Science Center at Tyler (UTHSCT)

80   were used for this study. Four to five weeks old mice were irradiated at a dose of 100cgy/mouse

81   for myeloablation. This was followed 6 hours later by intravenous (IV) inoculation with 2×10^5

82   human CD34$^+$ hematopoietic stem cells (STEMCELL technologies, Vancouver, Canada) per

83   mouse for humanization.

84   At 16 weeks after inoculation with human CD34$^+$ cells, humanization was confirmed in

85   accordance with a previously stablished protocol. Briefly, the whole blood samples were collected

86   by puncture of the submandibular vein and density gradient was used to separate peripheral blood

87   mononuclear cells (PBMCs). Once PBMCs were obtained, flow cytometry for specific human and

88   mouse immune cell markers was performed and humanization was confirmed for 13 mice. The

89   criteria for humanization included a positive human/mouse leukocyte ratio, as determined by

90   human CD45$^+$ vs. mouse CD45$^+$ expression, as well as the presence of multiple human immune

91   cell subsets, determined by markers for T-cells (CD3$^+$), B-cells (CD20$^+$), monocytes (CD14$^+$) and

92   natural killer (NK) cells (CD56$^+$), in accordance with a previously stablished protocol in our lab[13].

93   **Animal infection and experimental design**

94   Once mouse humanization was confirmed, the animals were randomly divided into 4

95   experimental groups (Figure 1A): A) No infection (n=3), B) HIV single infection (n=3), C) *Mtb*

96   single infection (n=3) and D) HIV/*Mtb* coinfection (n=4). Animals in groups C and D were infected

97   with aerosolized *Mtb*, H37Rv strain, using a Madison chamber[13,15]. Three non-humanized mice

98   were included in the infection chamber to confirm the infection dose. These three mice were

99   euthanized the following day and lung samples were collected, macerated and plated in 7H10

100   plates, supplemented with OADC (BD biosciences, Franklin Lakes, NJ). These mice confirmed

101   that the infection was successful, and the dose was determined to be ~40 CFU/lung.

102   Two days after the *Mtb* infection was carried out, mice in groups B and D were injected

103   intraperitoneally (IP) with 10^7 TCID of HIV-1 BaL strain (obtained from NIH AIDS Reagent

104   Program). Two weeks after inoculation, whole blood sample was obtained and RNA was extracted

105   from plasma sample of these mice, using the NucleoSpin RNA isolation kit (Macherey-Nagel,

106   Allentown, PA), according to manufacturer's instructions. The viral RNA load in each animal was

107   determined by RT-qPCR, using a control standard (obtained from NIH AIDS Reagent Program)

108   with known quantities of HIV-1 genome copies, as previously described[16]. All HIV-inoculated

109   mice were positive for HIV RT-qPCR and showed similar viral RNA loads.

110   Three weeks after infection, all animals were humanely euthanized, in accordance with the

111   NIH guidelines for euthanasia of rodents using carbon dioxide, followed by confirmation by neck

112   dislocation. During necropsy, lung samples from each mouse were collected in accordance with

113   previous protocols. Briefly, once euthanasia was confirmed, the thoracic cavity was opened, and

114   the lungs were perfused and inflated by injection of 10% neutral buffered formalin (Thermo

115   Scientific, Waltham, MA) into the right heart ventricle and trachea, respectively. Afterwards,

116   samples were immediately submerged in the same buffer and kept at 4 °C until paraffin

117   embedding[17,18]. All animal procedures were approved by the UTHSCT Institutional Animal Care

118   and Use Committee (IACUC) (Protocol #763).

119   **10x Visium spatial transcriptome assay:**

120   Formalin fixed and paraffin embedded tissue sections were used to prepare sample slides

121   as per the 10x Genomics protocol (CG000518 and CG000520). RNA was isolated from the FFPE

122   sections using RNeasy FFPE kit (Qiagen, # 73504) following the kit protocol. Samples with

123   DV200 value of > 30% were selected for the spatial transcriptomics assay. The qualified samples

124   after H&E staining and image were decrosslinked based the protocol (CG000520) and the

125   sequencing libraries were prepared as per the manufacturer's protocol (CG000495). The quality of

126   the final libraries was examined using Agilent High Sensitive DNA Kit (#5067-4626) using

127   Agilent Bioanalyzer 2100 (Agilent Technologies, Santa Clara, USA). The qualified libraries were

128   sequenced using the paired-end sequencing on an Illumina Novaseq System (Illumina, Inc., USA).

129   **Visium spatial sequencing data analysis:**

130   With demultiplexed sequence fastq files and CytAssist tissue image as input, Space ranger

131   was used to map the reads to the latest human genome (hg38) and quantified read counts per spot.

132   The counts were normalized using 'sctranform' method in Seurat package[19]. For comparison

133   between different samples, the data was further normalized using minimum median counts

134   function. The samples were clustered and projected on UMAP. Find markers function was used

135   for identifying cluster specific markers and differentially expressed genes. Genes exhibiting a

136   minimum |log2FC| value of 2 at p.adj value of <0.05 were considered differentially expressed

137   genes. Pathway analysis was performed using GprofileR[20]. Loupe browser was used to examine

138   the spot-wise expression level of individual genes. Deconvolution of spatial gene expression

139   profiles were performed using RCTD package[21]. Single cell RNA sequencing (GSE192483) of

140   lung tissues with 18F-FDG avidity and nearby uninvolved tissues from six tuberculosis patients[22]

141   were used as reference for deconvolution analysis. Azimuth[23] was used for annotating the cells in

142   the reference dataset. Visualizations were created using ggplot2 package in R environment (4.1.1).

143   **Results**

Immune cell infiltration patterns in the lungs are different for each infection type:

144

145   We first investigated the effect of HIV and *Mtb* coinfection on immune responses in the

146   lung. In our earlier study on humanized mice model of coinfection, we observed that the CD4$^+$ T

147   cells depletion occurred rapidly after day 15 post infection and plateaued after day 28. Therefore,

148   to investigate the status of immune responses during rapid declining of CD4$^+$ cells, we euthanized

149   mice 21 days post infection and performed spatial transcriptome analysis of lung specimens from

150   humanized mice with HIV infection, *Mtb* infection and coinfection using 10x Genomics Visium

151   platform. The "No infection" group was used as control (Figure 1A). Excluding the poor-quality

152   regions and empty spots, our spatial transcriptomics analysis detected expression of 18,000 genes

153   across 3633, 2698, 2778, and 1397 spots in no infection, HIV, *Mtb*, and coinfection lungs,

154   respectively.

155   Since TB is predominantly a lung infectious disease, we assume that examining the

156   frequency of infiltration of different immune cells into lung will help us understand the immune

157   response against the pathogen. CD4$^+$ cells play crucial role in mitigating *Mtb* infection by releasing

158   signals that stimulate B cells to produce antibodies, cytotoxic T cells to kill infected cells, and

159   macrophages to engulf and destroy pathogen. Therefore, we were also interested in understanding

160   the effect of declining CD4$^+$ T cells titer on immune cell infiltration in lung tissues during

161   coinfection. To compare the abundance of immune cell markers across all 4 infections groups, we

162   normalized the spatial gene expression data from all samples using sctranform method followed

163   by recorrecting the SCT counts minimum median counts. This data is suitable for comparing the

164   gene expression between samples. As shown in Figure 1B, we observed that expression of CD4 is

165   minimal in HIV single infection and in coinfection compared to control and *Mtb* single infection.

166   This is expected as HIV infection and coinfection depletes CD4$^+$ T cell population. These results

167   suggest the possibility of existence of infection specific immune cell infiltration landscape in the

168   lungs.

169   To further investigate infiltration frequencies of immune cells into lungs across different

170   infection groups and control, we performed RCTD based cell type deconvolution analysis by

171   integrating the previously published single cell RNA sequencing data of human lung granuloma

172   (as detected by PET-CT) and their matched normal tissues of TB patients with our spatial

173   transcriptome data of all 4 infection groups. We first annotated the cell type labels of all cells in

174   scRNAseq data using Azimuth annotation database at the finest annotation level and transferred

175   these labels to our spatial transcriptome data during deconvolution analysis in 'full mode'. Since

176   Visium spots may span up to 6 individual cells, we opted to run deconvolution in 'full mode' as it

177   allows identification of any number of cells existing in each pixel. Corroborating with CD4 gene

178   expression in the tissues, cell type weights for CD4$^+$ T cells also showed the highest abundance of

179   CD4$^+$ T cells in *Mtb* infection while showing less abundance in HIV and coinfection mice (Figure

180   1C). Supporting previous reports, CD4$^+$ cells were less coinfection mice compared to HIV single

181   infection[24] (Figure 1C). Surprisingly, the abundance of nonclassical monocytes reduced in all

182   infections compared to control (Figure 1C). NK cells abundance was less in the coinfection mice

183   compared to the rest of the three groups. NK cell abundance was the highest in *Mtb* single infection

184   lung (Figure 1C). The lower levels of NK cell infiltration in coinfection compared to *Mtb* single

185   infection were observed in an earlier study[24]. The distribution of cell type weights of myeloid

186   lineage cells such as alveolar macrophages, CCL3$^+$ alveolar macrophages, classical monocytes,

187   monocyte derived macrophages, interstitial macrophages was similar across all groups suggesting

188   that infection status has minimal or no effect in the infiltration of these cells (Figure S1).

189   Altogether, these results suggest that lung tissue infiltration of various immune cell types depend

190   on the type of infection.

191   **Lung immune cell infiltration patterns differ based on infection status as well as local**

192   **histological milieu**

193   To understand the distinct patterns of immune cell infiltration into lungs, we performed

194   clustering of Visium spots across all 4 infection states together using Uniform Manifold

195   Approximation and Projection (UMAP) based on 50 principal components at a resolution of 0.9.

196   We observed a total of 14 clusters across 4 samples with no infection (12), HIV (11), *Mtb* (12),

197   and coinfection (12) (Figure 2A, S2A). Clusters 0-11 were present in all 4 samples while cluster

198   12 was detected neither in HIV nor in coinfection. Interestingly, cluster 13 was detected

199   exclusively in the coinfection group (Figure 3, S2A).

200   Interestingly, UMAP projection (Figure 2A) revealed a broad separation of all 14 clusters

201   into 3 distinct groups. These three cluster groups are represented by all four infection groups

202   (Figure 2A). Majority of the clusters, including clusters 0-3, 5-8, 10, 11 and 13 (total 11 clusters)

203   were placed together on the right on UMAP projection as a single large group (Figure 2B). These

204   spots correspond to alveolar/interstitial compartment of the lung across all 4 infection categories

205   (Figure 2B, S2B). Therefore, we aggregated these 11 clusters into one large cluster namely

206   'alveolar/interstitial' cluster for further analysis. Clusters 4 and 12 were placed separately together

207   and far from alveolar/interstitial cluster on UMAP projection (Figure 2C; represented in green and

208   blue, respectively). These spots belong to areas spanning airways in all four lungs (Figure S2C;

209   represented in green and blue, respectively). Therefore, we combined clusters 4 and 12 into one

210   cluster called 'airway_1' (Figure S2C; represented in red). Similarly, cluster 9, another distinct

211   cluster far away from the rest on the UMAP projection also harbored spots representing airways

212   across all four groups. It was also renamed as 'airway_2' for further analysis. Although, both

213   airway-1 and airway_2 clusters represent airways, they were not combined because they appeared

214   distinct from each other on UMAP projection. Interestingly, clusters were separated based on tissue

215   location and histological features rather than infection status. Altogether, these results suggest that

216   immune infiltration is strongly influenced by histological features compared to infection status in

217   our study.

218   To investigate the immune infiltration pattern differences between different clusters

219   associated with different histological location, we used the cell type weights obtained in

220   deconvolution analysis described in Figure 1. Abundance of $CD4^+$ T cells varied marginally

221   between alveolar/interstitial, airway_1, and airway_2 clusters with alveolar/interstitial and

222   airway_2 clusters exhibiting high abundance compared to airway_1 (Figure S2D). In contrast, the

223   abundance of monocyte derived macrophages was high in airway-1 compared to the rest (Figure

224   S2D). Interestingly, airway-2 cluster is enriched with $CCL3^+$ alveolar macrophages which are

225   known to be effective in phagocytosis of bacteria and other antigens (Figure 2D)[25] whereas

226   alveolar macrophages without high expression of CCL3 were marginally more abundant in

227   airway_1 cluster (Figure 2D). In contrast, airway_2 cluster and alveolar/interstitium clusters

228   exhibited a lower abundance of nonclassical monocytes compared to the airway_1 (Figure 2D).

229   Alveolar/interstium cluster is enriched with $CD8^+$ T cells and classical monocytes while

230   type 2 dendritic cells were less (Figure 2D). B cell, mast cells and type 1 dendritic cells did not

231   show any difference in abundance among the three clusters (Figure S2E). Altogether, these results

232   suggest that different histological regions may harbor district immune cell types. However, it is

233   not clear whether this differential abundance contributes to different immune responses.

Cellular organization and composition of lymphoid cell aggregates markedly different from typical mature tuberculosis granuloma

Several previous studies investigated the cellular architecture of mature tuberculosis granuloma. Granuloma may appear as a tiny lymphoid cell aggregate at initial stages and will progress into a non-necrotic or central necrotic mature granuloma. Our understanding of the cellular architecture of lymphoid cell aggregates is limited compared to mature granuloma. Examination of hematoxylin (H&E) staining revealed the presence of a lymphoid aggregate in the region of tissue subjected to spatial transcriptome profiling from coinfection mice. Focusing exclusively on this region, we investigated 1) whether the cellular architecture of lymphoid aggregate is similar or different from the mature granuloma, and 2) whether the lymphoid aggregates show any transcriptomic changes characteristic of mature granuloma.

Surprisingly, we noticed that spots belonging to cluster 13, the only cluster on UMAP that was exclusively detected in coinfection, spanned the entirety of the lymphoid cell aggregate in this sample, suggesting that this lymphoid aggregate exhibit distinct transcription program compared to the rest of the tissues across all 4 infection groups (Fig 3A). This lymphoid aggregate is present in the interstitial region adjacent to a large airway and appears to have densely populated infiltrated lymphoid cells on H& E staining (Fig 3B). On UMAP projection, cluster 13 is located together within all clusters spanning interstitial region yet appears distinct from the rest of all interstitial clusters (Figure 3C).

Necrotic granulomas are structured around a central core of necrotic cell debris in which much of the bacteria are concentrated. The layers adjacent to necrotic core are mainly composed of macrophages[2]. Layers of epithelioid macrophages surround the necrotic core interspersed with other macrophage populations such as classical alveolar macrophages, monocyte derive

257   macrophages, lipid laden foamy macrophages, and giant cell[2]. A diversity of other immune cell

258   types is seen at the periphery as well as within the epithelioid layers of the granuloma. Non-

259   necrotic granulomas have similar structural arrangement except that they do not have necrotic

260   core[2]. However, cellular architecture and dynamics of these lymphoid aggregates are poorly

261   understood.

262   To decipher the cell type abundances in the Visium spots spanning the lymphoid cell

263   aggregate, we extracted cell type frequency predictions obtained from RCTD deconvolution

264   analysis. We labeled spots spanning the lymphoid cell aggregate as inner/core region, edge and

265   periphery, beginning from the center to the outer region (Figure 3D). To compare the abundance

266   of different immune cells predicted based on deconvolution analysis, we plotted a heatmap with

267   hierarchical clustering gene wise and spot wise (Figure 3E). Interestingly, we observed that the

268   spot wise clustering as shown by the column dendrogram separated peripheral spots from the inner

269   and edge spots accurately suggesting that cell distribution in these compartments is stratified based

270   on the location. In mature granuloma, B cells are present in the periphery while being absent or

271   minimal in the core. In contrast, we observed that in lymphoid aggregate, inner/core region spot is

272   highly abundant in B cells (Figure 3E). High abundance of B cells in the core region of the

273   lymphoid aggregate was also confirmed by the highest abundance of the mature B cell markers

274   like CD19 (Figure 3F), CD20 (MS4A1) (Figure S3A), and IgM (IGHM) (Figure S3B).

275   Plasmacytoid DCs are also highly enriched in the core and edge regions as shown in the heatmap

276   (Figure 3E), and corroborating with expression of plasmacytoid markers such as CD123 (IL3RA)

277   (Figure 3G), and CD303 (CLEC4C) (Figure S3C). Similarly, lymphoid aggregate harbors

278   nonclassical monocytes abundantly (Figure 3E). Nonclassical monocytes express high levels of

279   CD97 (ADGRE5), P2RX1, and Siglec10[26]. As expected, we observed a high abundance of CD97

280   (ADGRE5) (Figure S3D), P2RX1 (Figure S3E), and Siglec10 (Figure S3F) in the core or edge of

281   the lymphoid aggregate while their abundance being less in the periphery. We also observed

282   enrichment of plasma cells, DC2, CD4 T cells and nonclassical monocytes in the core of the lesion

283   (Figure 3E). In contrast, we observed NK cells, mast cells, macrophages, CD8 T cells, DC1 cells,

284   and classical monocytes on the periphery (Figure 3E).

285   Altogether, these results suggest that lymphoid cell aggregates may not essentially

286   originate with macrophage cells predominantly at the core. We speculate that granuloma

287   architecture may evolve into macrophage laden core and lymphocyte abundant periphery overtime.

288   **Lymphoid cell aggregates exhibited gene expression changes characteristic of granulomas**

289   Given that lymphoid cell aggregates did not show cellular architecture akin to granuloma,

290   we checked whether this lesion exhibits any transcriptomic changes seen in mature granulomas.

291   We examined the expression of genes that are part of gene sets related to granuloma in Molecular

292   Signatures Database (MSigDB). We analyzed the HP_GRANULOMA gene set consisting of

293   ACP5, CYBB, CYBC1, DNASE2, DOCK2, IRF8, NF1, and PIK3CG. Aggregated expression of

294   these genes was higher in the lymphoid aggregate region (Figure 4A) compared to the rest of the

295   lung tissue while individual genes also exhibited relatively high expression in the lymphoid

296   aggregate region (Figure S4). Similarly, another gene set named HP_ GRANULOMATOSIS

297   consisting of ASAH1, CTLA4, CYBA, CYBB, HLA-DPA1, HLA-DPB1, NCF1, NCF2, PRTN3,

298   and PTPN22 also exhibited higher expression in lymphoid aggregate compared to rest of the tissue

299   (Figure 4A, S5A). These results suggest that gene expression changes characteristic of mature

300   granulomas appear to emerge early into the development of the granuloma from lymphoid

301   aggregate.

302   Encouraged by these results, to understand the molecular changes occurring early stages

303   of the granuloma development, we performed pathway analysis to identify signaling pathways

304   enriched in the lymphoid cell aggregate region. We performed differential expression analysis

305   using Seurat 'find-markers' function to identify genes that were up or downregulated in cluster 13.

306   At a log2FC cut off 2 and p.adj value of 0.05, we detected 383 upregulated and 20 downregulated

307   genes. Pathway analysis was performed independently for both up and down-regulated genes.

308   Multiple pathway terms representing immune response to viral, *Mtb*, and bacterial infections, B

309   cell and NK cell activity, cytokine signaling, glucose metabolism and oxidative phosphorylation,

310   ROS generation, interferon signaling and activation of several Interferon regulatory factor

311   transcriptional factors were significantly enriched in genes upregulated in the lymphoid cell

312   aggregate (Figure 4B, Supplementary Table 1). Interestingly, oxidative phosphorylation and ROS

313   generation are crucial for pathogen killing inside granulomas[27]. Transcriptional targets of several

314   interferon regulatory factors (IRF5, IRF7, and IRF9) were enriched in upregulated genes (Figure

315   4B-C, Supplementary Table 1). Type I-interferon signaling is known to promote *Mtb* infection by

316   facilitating the release of neutrophil extracellular traps[28] and suppressing interferon gamma and

317   interleukin 1α/β signaling[29].

318   Intriguingly, similar analysis on downregulated genes revealed enrichment of multiple

319   pathways related to downregulation of inhibitory SMAD expression in lymphoid cell aggregate

320   suggesting that this lesion may harbor activated TGFβ signaling (Figure 4D, Supplementary Table

321   2). This was corroborated by decreased expression of SMAD6 which inhibits TGFβ signaling and

322   upregulation of TGFβ signaling ligands namely TGFβ1/2 in the same tissue region, suggesting that

323   TGFβ signaling is activated (Figure 4E). Altogether, these results suggest that lymphoid cell

324   aggregates may show several characteristics of granulomas even before they evolve into mature

325   granulomas.

Discussion

327   Novel spatial transcriptomic technologies provide a powerful tool to assess molecular and

328   immunological changes in situ in various tissues, thus understanding the effects of infection on the

329   host and allowing for in-depth knowledge of how disease is developed or avoided[30,31]. In the

330   present study, these technologies were used to evaluate the early changes caused by HIV and *Mtb*

331   infections and coinfection in humanized mouse lung tissues. Although lung is the main target organ

332   for *Mtb*, it's also greatly affected by the generalized immunosuppression caused by HIV[9] due to

333   massive depletion of CD4$^+$ T cell population[8,9]. The increase in CD4$^+$ T cells after *Mtb* single

334   infection relates to increased migration to the affected sites to control the pathogens[4]. Meanwhile,

335   the severe local depletion of this CD4+ T cell subset in HIV-infected hu-mice (with or without *Mtb*

336   coinfection) is a staple of HIV that has been previously described[8] and found in the present work.

337   The approach used in the present study allowed for the detection of alterations in less studied

338   populations, mainly non-classical monocytes and NK cells. Interestingly, even though HIV and

339   *Mtb* single infection increased the NK cell population, when compared to the uninfected control,

340   coinfection had the opposite effect. A similar pattern was reported for certain phenotypes of NK

341   cells in HIV/*Mtb* coinfected patients and it is likely that alterations in this cell subset vary in

342   accordance with the phenotypes differentiated in the subject[32].

343   A considerable portion of the differences evidenced in cell populations presented in the

344   tissue corresponded not only with infection, but rather with different histological regions, with

345   areas including bronchi and major airways being clearly differentiated from interstitial tissue.

346   However, even within the clustered airway regions, viral and bacterial infection modified the

347   phenotypical landscape. This is shown by the high presence of alveolar macrophages expressing

348   CCL3 in the airway regions from all the infected animals, in contrast with the uninfected controls.

349   CCL3 is known to aid in the activation of alveolar macrophages and efforts to control bacterial

350   and viral pathogens[25,33]. Recently, it was also found to be increased in COVID-19 patients suffering

351   alveolar damage, supporting the important role of these cells for pulmonary immunity[34].

352   The finding of a structurally organized and clearly differentiated cell cluster with a unique

353   transcriptomic profile, in the sample from HIV/*Mtb* coinfected mouse, provides insight into the

354   early phenotypical and signaling changes induced by this type of infection. Spatial analysis showed

355   the presence of both lymphoid and myeloid cells in the lymphoid aggregates. Remarkably, despite

356   being infected with HIV and showing generalized CD4$^+$ T cell depletion in the tissue, this cell

357   subset was found within the structure, mainly in the inner part and accompanied by B cells and

358   plasmacytoid DCs. It should be noted that the manner in which the cell subsets are organized in

359   the lymphoid structure found in the HIV/*Mtb* coinfected sample is not compatible with that found

360   in mature granulomas, which generally have a necrotic core, surrounded by macrophages and

361   epithelioid cells with lymphocytes in the outer layer[2,3,7]. Conversely, the unique structure found in

362   the HIV/*Mtb* coinfected hu-mouse tissue lacks evidence of necrosis and the monocytic cells within

363   it are in the outer layer. This is likely due to the fact that this cell aggregate is in the early stages

364   of forming a granulomatous structure and the time after infection has not yet been sufficient to

365   generate necrosis. This is in line with previous findings in murine *Mtb* model which detected the

366   presence of inflammatory cell aggregates, mainly adjacent to circulation or bronchi as early as 2

367   weeks after infection, with the first necrotic changes being detected around 1 month after

368   infection[35,36]. Moreover, our results show that the transcriptomic alterations found in this

369   premature granuloma-like structure are compatible with the signaling reported for mature

370   granulomas, supporting the idea that the lymphoid aggregate found in this sample is in the early

371   stages of granuloma formation.

372   The process of granuloma establishment involves precise modulation of the interferon

373   pathway, mainly through the upregulation of multiple IRFs, as shown in the cells present in this

374   granuloma-like structure. Some of the IRF genes found to be upregulated in the lymphoid

375   aggregate from the present study have been previously reported to be crucial for granuloma

376   formation and maintenance, as IRF8 deficient mice proved unable to form these structures and

377   limit *Mtb* growth after infection[37]. However, the increased transcription of different IRF genes

378   suggests regulation of the IFN response using multiple mechanisms, including cell differentiation

379   and innate immunity. This is likely a response to the initial induction of type-I IFNs and activation

380   of the IFN pathway and IFN stimulated genes (ISGs) after infection, but the relevance of this

381   multiple approach to IFN modulation in more advanced stages of structural remodeling remains to

382   be elucidated. Reports suggest that mature granulomas (after 9 weeks post infection) do not show

383   upregulation of these pathways, while others report increased IRF transcription in these structures,

384   though mainly in non-immune cell types (fibroblasts)[6,38].

385   Consequently, the activation of immune response by the IFN pathway leads to increased

386   energy requirements in the immune cells present in the lymphoid aggregate, as exemplified by the

387   upregulation of oxidative phosphorylation related genes. This has been established as an important

388   metabolic consequence of both HIV and *Mtb* infections, as well as HIV/*Mtb* coinfection[39-41]. Our

389   results show that the generalized metabolic changes induced by HIV/*Mtb* coinfection also occurs

390   locally in the affected tissues and, specifically in the affected areas, starting at an early stage of the

391   infection.

392   In addition, contrasting with the regulation of the IFN pathway, our results show a lack of

393   TGFβ regulation. TGFβ inhibition of *Mtb*-specific CD4^{+} T cells has been found to play a role in

394   the maintenance of *Mtb* within mature granuloma structures in rhesus macaque and mice models[42].

395   This cytokine and its associated pathways has also been proposed as a determinant of myeloid cell

396   differentiation in TB granulomas[43], while virtual modeling results have suggested an enhancement

397   of bacterial clearance in absence of TGFβ[44].

Conclusions

399   The modulation of immune response by pathogens is an important determinant for the

400   outcome of infection. This can take the form of generalized immunosuppression, as caused by

401   HIV, or more nuanced modulation of immune response, as induced by *Mtb*. The results from the

402   present study show the effects of these pathogens, whether in single infection or coinfection, in

403   lung tissue of a humanized mouse model at an early timepoint after inoculation. Our findings

404   suggest that alterations in cellular infiltration and structural remodeling of the tissue begin to take

405   place early after infection and closely resemble those that have been previously reported for

406   humans and other animal models. This further validates the use of the NSG-SGM3-IL15 mouse

407   strain as a reliable animal model that can reproduce multiple aspects of HIV and *Mtb* infections,

408   as well as HIV/*Mtb* coinfection. Nevertheless, future studies, using higher resolution spatial

409   transcriptomics, will further elucidate the transcriptomic changes in lung immune cell populations

410   at a single cell level. This information will provide further detail into specific changes in different

411   cell populations, both in terms of phenotype and signaling and open up new avenues of research

412   to generate intervention strategies that improve infection outcome in patients infected with HIV

413   and *Mtb*.

Conflict of interest:

427   **References**

428   1   WHO. Global Tuberculosis Report. (WHO, Geneva, Switzerland, 2023).

429   2   Cronan, M. R. In the Thick of It: Formation of the Tuberculous Granuloma and Its
430   Effects on Host and Therapeutic Responses. *Frontiers in Immunology* **13** (2022).
431   https://doi.org:10.3389/fimmu.2022.820134

432   3   McCaffrey, E. F. *et al.* The immunoregulatory landscape of human tuberculosis
433   granulomas. *Nat Immunol* **23**, 318-329 (2022). https://doi.org:10.1038/s41590-021-
434   01121-x

435   4   Bromley, J. D. *et al.* CD4(+) T cells re-wire granuloma cellularity and regulatory
436   networks to promote immunomodulation following Mtb reinfection. *Immunity* **57**,
437   2380-2398 e2386 (2024). https://doi.org:10.1016/j.immuni.2024.08.002

438   5   Carow, B. *et al.* Spatial and temporal localization of immune transcripts defines
439   hallmarks and diversity in the tuberculosis granuloma. *Nat Commun* **10**, 1823 (2019).
440   https://doi.org:10.1038/s41467-019-09816-4

441   6   Krausgruber, T. *et al.* Single-cell and spatial transcriptomics reveal aberrant lymphoid
442   developmental programs driving granuloma formation. *Immunity* **56**, 289-306 e287
443   (2023). https://doi.org:10.1016/j.immuni.2023.01.014

7   Qiu, X. *et al.* Spatial transcriptomic sequencing reveals immune microenvironment features of Mycobacterium tuberculosis granulomas in lung and omentum. *Theranostics* **14**, 6185-6201 (2024). https://doi.org:10.7150/thno.99038

8   Foreman, T. W. *et al.* CD4 T cells are rapidly depleted from tuberculosis granulomas following acute SIV co-infection. *Cell Rep* **39**, 110896 (2022). https://doi.org:10.1016/j.celrep.2022.110896

9   Kaushal, D., Singh, D. K. & Mehra, S. Immune Responses in Lung Granulomas during Mtb/HIV Co-Infection: Implications for Pathogenesis and Therapy. *Pathogens* **12** (2023). https://doi.org:10.3390/pathogens12091120

10   Azevedo-Pereira, J. M. *et al.* HIV/Mtb Co-Infection: From the Amplification of Disease Pathogenesis to an "Emerging Syndemic". *Microorganisms 2023, Vol. 11, Page 853* **11** (2023-03-27). https://doi.org:10.3390/microorganisms11040853

11   Bohorquez, J. A., Jagannath, C., Xu, H., Wang, X. & Yi, G. T Cell Responses during Human Immunodeficiency Virus/Mycobacterium tuberculosis Coinfection. *Vaccines (Basel)* **12** (2024). https://doi.org:10.3390/vaccines12080901

12   Sawyer, A. J. *et al.* Spatial mapping reveals granuloma diversity and histopathological superstructure in human tuberculosis. *J Exp Med* **220** (2023). https://doi.org:10.1084/jem.20221392

13   Bohorquez, J. A. *et al.* A Novel Humanized Mouse Model for HIV and Tuberculosis Co-infection Studies. *bioRxiv*, 2024.2003.2005.583545 (2024). https://doi.org:10.1101/2024.03.05.583545

14   Lepard, M. *et al.* Comparing Current and Next-Generation Humanized Mouse Models for Advancing HIV and HIV/Mtb Co-Infection Studies. *Viruses* **14** (2022). https://doi.org:10.3390/v14091927

15   Feng, Y. *et al.* Exposure to Cigarette Smoke Inhibits the Pulmonary T-Cell Response to Influenza Virus and<i>Mycobacterium tuberculosis</i>. *Infection and Immunity* **79**, 229-237 (2011). https://doi.org:10.1128/iai.00709-10

16   Butler, S. L., Hansen, M. S. T. & Bushman, F. D. A quantitative assay for HIV DNA integration in vivo. *Nature Medicine* **7**, 631-634 (2001). https://doi.org:10.1038/87979

17   Morton, J. & Snider, T. A. Guidelines for collection and processing of lungs from aged mice for histological studies. *Pathobiology of Aging & Age-related Diseases* **7**, 1313676 (2017). https://doi.org:10.1080/20010001.2017.1313676

18   Davenport, M. L., Sherrill, T. P., Blackwell, T. S. & Edmonds, M. D. Perfusion and Inflation of the Mouse Lung for Tumor Histology. *J Vis Exp* (2020). https://doi.org:10.3791/60605

19   Hao, Y. *et al.* Dictionary learning for integrative, multimodal and scalable single-cell analysis. *Nat Biotechnol* **42**, 293-304 (2024). https://doi.org:10.1038/s41587-023-01767-y

20   Kolberg, L., Raudvere, U., Kuzmin, I., Vilo, J. & Peterson, H. gprofiler2 -- an R package for gene list functional enrichment analysis and namespace conversion toolset g:Profiler. *F1000Res* **9** (2020). https://doi.org:10.12688/f1000research.24956.2

21   Cable, D. M. *et al.* Robust decomposition of cell type mixtures in spatial transcriptomics. *Nat Biotechnol* **40**, 517-526 (2022). https://doi.org:10.1038/s41587-021-00830-w

488   22   Wang, L. *et al.* Single-cell RNA-sequencing reveals heterogeneity and intercellular
489   crosstalk in human tuberculosis lung. *J Infect* **87**, 373-384 (2023).
490   https://doi.org:10.1016/j.jinf.2023.09.004
491   23   Hao, Y. *et al.* Integrated analysis of multimodal single-cell data. *Cell* **184**, 3573-3587
492   e3529 (2021). https://doi.org:10.1016/j.cell.2021.04.048
493   24   Xiao, G. *et al.* Uncovering the Bronchoalveolar Single-Cell Landscape of Patients With
494   Pulmonary Tuberculosis With Human Immunodeficiency Virus Type 1 Coinfection. *J*
495   *Infect Dis* **230**, e524-e535 (2024). https://doi.org:10.1093/infdis/jiae042
496   25   Lindell, D. M., Standiford, T. J., Mancuso, P., Leshen, Z. J. & Huffnagle, G. B.
497   Macrophage inflammatory protein 1alpha/CCL3 is required for clearance of an acute
498   Klebsiella pneumoniae pulmonary infection. *Infect Immun* **69**, 6364-6369 (2001).
499   https://doi.org:10.1128/IAI.69.10.6364-6369.2001
500   26   Wong, K. L. *et al.* Gene expression profiling reveals the defining features of the
501   classical, intermediate, and nonclassical human monocyte subsets. *Blood* **118**, e16-
502   31 (2011). https://doi.org:10.1182/blood-2010-12-326355
503   27   Song, E. *et al.* Chronic granulomatous disease: a review of the infectious and
504   inflammatory complications. *Clin Mol Allergy* **9**, 10 (2011).
505   https://doi.org:10.1186/1476-7961-9-10
506   28   Chowdhury, C. S. *et al.* Type I IFN-mediated NET release promotes Mycobacterium
507   tuberculosis replication and is associated with granuloma caseation. *Cell Host*
508   *Microbe* **32**, 2092-2111 e2097 (2024). https://doi.org:10.1016/j.chom.2024.11.008
509   29   Donovan, M. L., Schultz, T. E., Duke, T. J. & Blumenthal, A. Type I Interferons in the
510   Pathogenesis of Tuberculosis: Molecular Drivers and Immunological Consequences.
511   *Front Immunol* **8**, 1633 (2017). https://doi.org:10.3389/fimmu.2017.01633
512   30   Marx, V. Method of the Year: spatially resolved transcriptomics. *Nat Methods* **18**, 9-14
513   (2021). https://doi.org:10.1038/s41592-020-01033-y
514   31   Williams, C. G., Lee, H. J., Asatsuma, T., Vento-Tormo, R. & Haque, A. An introduction
515   to spatial transcriptomics for biomedical research. *Genome Med* **14**, 68 (2022).
516   https://doi.org:10.1186/s13073-022-01075-1
517   32   Gao, J. *et al.* Mtb/HIV co-infection immune microenvironment subpopulations
518   heterogeneity. *Int Immunopharmacol* **143**, 113341 (2024).
519   https://doi.org:10.1016/j.intimp.2024.113341
520   33   Sadee, W. *et al.* Human alveolar macrophage response to Mycobacterium
521   tuberculosis: immune characteristics underlying large inter-individual variability. *Res*
522   *Sq* (2023). https://doi.org:10.21203/rs.3.rs-2986649/v1
523   34   Garcia-Prieto, C. A. *et al.* Spatial transcriptomics unveils the *in situ* cellular and
524   molecular hallmarks of the lung in fatal COVID-19. *bioRxiv*, 2024.2007.2003.601404
525   (2024). https://doi.org:10.1101/2024.07.03.601404
526   35   Tsai, M. C. *et al.* Characterization of the tuberculous granuloma in murine and human
527   lungs: cellular composition and relative tissue oxygen tension. *Cell Microbiol* **8**, 218-
528   232 (2006). https://doi.org:10.1111/j.1462-5822.2005.00612.x
529   36   Driver, E. R. *et al.* Evaluation of a mouse model of necrotic granuloma formation using
530   C3HeB/FeJ mice for testing of drugs against Mycobacterium tuberculosis. *Antimicrob*
531   *Agents Chemother* **56**, 3181-3195 (2012). https://doi.org:10.1128/AAC.00217-12

532   37   Rocca, S. *et al.* Interferon regulatory factor 8-deficiency determines massive
533   neutrophil recruitment but T cell defect in fast growing granulomas during
534   tuberculosis. *PLoS One* **8**, e62751 (2013).
535   https://doi.org:10.1371/journal.pone.0062751
536   38   Mehra, S. *et al.* Granuloma correlates of protection against tuberculosis and
537   mechanisms of immune modulation by Mycobacterium tuberculosis. *J Infect Dis*
538   **207**, 1115-1127 (2013). https://doi.org:10.1093/infdis/jis778
539   39   Herbert, C., Luies, L., Loots, D. T. & Williams, A. A. The metabolic consequences of
540   HIV/TB co-infection. *BMC Infectious Diseases* **23** (2023).
541   https://doi.org:10.1186/s12879-023-08505-4
542   40   Masson, J. J. R. *et al.* Assessment of metabolic and mitochondrial dynamics in CD4+
543   and CD8+ T cells in virologically suppressed HIV-positive individuals on combination
544   antiretroviral therapy. *PLOS ONE* **12** (30 ago 2017).
545   https://doi.org:10.1371/journal.pone.0183931
546   41   Singh, V. *et al.* Mycobacterium tuberculosis-Driven Targeted Recalibration of
547   Macrophage Lipid Homeostasis Promotes the Foamy Phenotype. *Cell Host & Microbe*
548   **12** (2012/11/15). https://doi.org:10.1016/j.chom.2012.09.012
549   42   Gern, B. H. *et al.* TGFβ restricts expansion, survival, and function of T cells within the
550   tuberculous granuloma. *Cell Host & Microbe* **29**, 594-606.e596 (2021).
551   https://doi.org:10.1016/j.chom.2021.02.005
552   43   Peters, J. M. *et al.* Systematic deconstruction of myeloid cell signaling in tuberculosis
553   granulomas reveals IFN-γ, TGF-β, and time are associated with conserved myeloid
554   diversity. *bioRxiv*, 2024.2005.2024.595747 (2024).
555   https://doi.org:10.1101/2024.05.24.595747
556   44   Warsinske, H. C., Pienaar, E., Linderman, J. J., Mattila, J. T. & Kirschner, D. E. Deletion
557   of TGF-beta1 Increases Bacterial Clearance by Cytotoxic T Cells in a Tuberculosis
558   Granuloma Model. *Front Immunol* **8**, 1843 (2017).
559   https://doi.org:10.3389/fimmu.2017.01843

560

561

562   **Figure legends**

563   **Figure 1. Cell type abundance variations between control, HIV, Mtb and coinfection mice as**

564   **predicted by cell specific marker analysis and cell type deconvolution analysis.**

565   A) The experimental protocol. The number of mice was four per group. B) Expression levels of

566   CD4 genes were shown across the four groups. D) Cell type weights for each spot in the samples

567   based on RCTD analysis were plotted for each infection types. X axis shows cell types weights

568   which are proportional to the cell type abundance in the tissue. Difference in cell weight

569   distributions was computed using Kruskal Wallis test followed by Dunn's test for pairwise

570   comparisons. P were adjusted for multiple hypothesis testing using Bonferroni correction method.

571   Significance levels are indicated as *P < .05, **P < .01, ***P < .001, and ****P < .0001. Figure

572   created using Biorender.com

573   **Figure 2. Identification clusters based on gene expression of all tissue spots from no infection,**

574   **HIV, Mtb, and coinfection mice lungs using Seurat package.**

575   A) Clusters from all four samples projected on UMAP and color based on cluster identifier (left)

576   and sample type (right). B) Alveolar/interstitium cluster (shown in blue), airway_1 (shown in

577   blue/green) and airway-2 (shown in red) clusters on UMAP projection. D) Cell type weights

578   obtained in RCTD deconvolution analysis were plotted for each cluster. Y axis shows cell types

579   weights which are proportional to the cell type abundance in the corresponding cluster. Color key

580   indicated the cluster identifier. Difference in cell weight distributions was computed using Kruskal

581   Wallis test followed by Dunn's test for pairwise comparisons. P values were adjusted for multiple

582   hypothesis testing using Bonferroni correction method. Significance levels are indicated as *$P <$

583   .05, **$P < .01$, ***$P < .001$, and ****$P < .0001$.

584 **Figure 3: Characterization of the unique cluster (cluster 13) detected in HIV/Mtb coinfection**

585 **mouse lung.**

586 A) Spatial mapping of cluster 13 which was detected exclusively in coinfection lung. Clusters were

587 identified on UMPA projection of all Visium spots passing quality control from all four infection

588 groups combined. Spots representing cluster 13 were highlighted in blue. B) Hematoxylin staining

589 of lung region matching with cluster 13 location in coinfection lung. This region contains a circular

590 lymphoid aggregate formed by dense lymphocyte infiltration located within the interstitial region

591 and close to two airways. C) UMAP projection of all Visium spots passing quality control from all

592 four infection groups highlighting the location of cluster 13. D) Projection of the Visium spots

593 overlapping with lymphoid aggregate shown in Figure 3B. The spots were labeled as core/inner

594 region, edge, and periphery depending on the location and were highlighted according to the label

595 with different colors. E) Heatmap showing the cell type abundances all the spots highlighted in

596 Figure 3D. Columns show individual spots spanning the lymphoid aggregate. The rows show the

597 immune cells detected in the spots. Color intensities represent the abundance of each cell in each

598 spot. Row and column dendrograms represent the similarity between cell abundances and

599 individual spots, respectively, as computed using hierarchical clustering. F) Spatial map of

600 expression of CD19, a mature B cell marker within and around the lymphoid aggregate. Spot-wise

601 gene expression data was projected on hematoxylin staining image of the lung tissue. Color key

602 represent the level of transcript expression. G) Expression of CD123 (IL3RA), plasmacytoid

603 markers in the same region as described for Figure 3F.

604 **Figure 4: gene expression changes and pathway analysis of lymphoid aggregate**
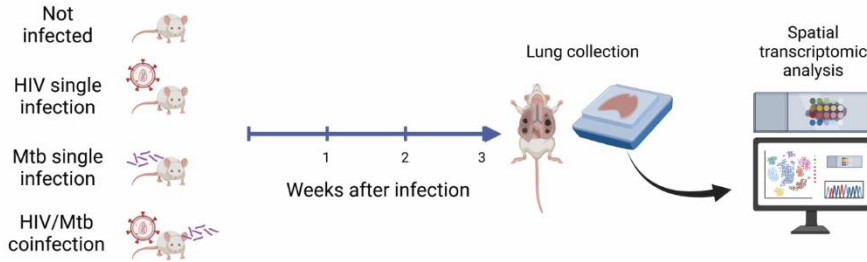
605 A) Aggregated gene expression of granuloma and granulomatosis gene sets from MSigDB

606 projected on hematoxylin stain of lungs from coinfection mice. Spot-wise gene expression

607 aggregate was projected on lymphoid cell aggregate and its surround tissue. Color key represents

608 aggregate of expression values of all the genes in the granuloma gene set (DOCK2, CYBC1,

609 PIK3CG, CYBB, IRF8, NF1, DNASE2, and ACP5) and granulomatosis gene set (DOCK2,

610 CYBC1, PIK3CG, CYBB, IRF8, NF1, DNASE2, and ACP5). B) Top 20 pathways based on p.adj

611 identified in over representation analysis on genes upregulated in cluster 13 spanning lymphoid

612 cell aggregate in coinfection mice. Gene ratios were computed with the percentage of total DEGs

613 in the given pathway term. C) Expression levels of interferon regulatory factors enriched among

614 upregulated genes in lymphoid cell aggregate were projected individually on lymphoid cell

615 aggregate and its surround tissue. D) Top 20 pathways identified in over representation analysis

616 on gene down regulated in cluster 13 as shown like figure 4B. E) Down regulation of SMAD6, an

617 inhibitory SMAD and upregulation of TGFB1/2 in lymphoid cell aggregate. Gene expression

618 levels quantified in spatial transcriptomics analysis were projected on hematoxylin-stained tissue

619 section. A, C, E) Color key represents aggregate/individual gene expression values in log2 scale.
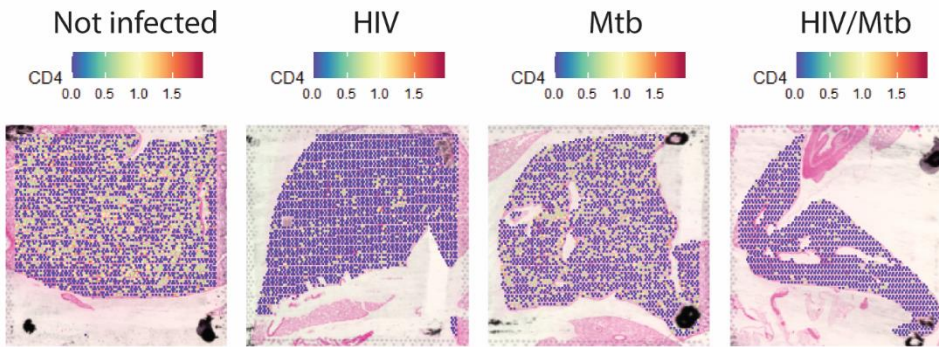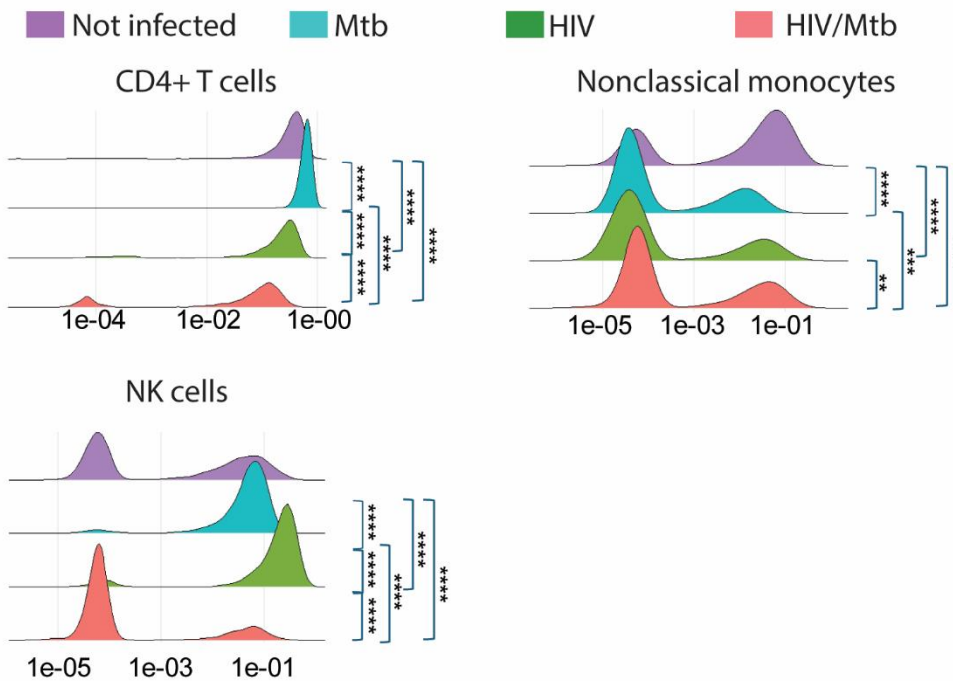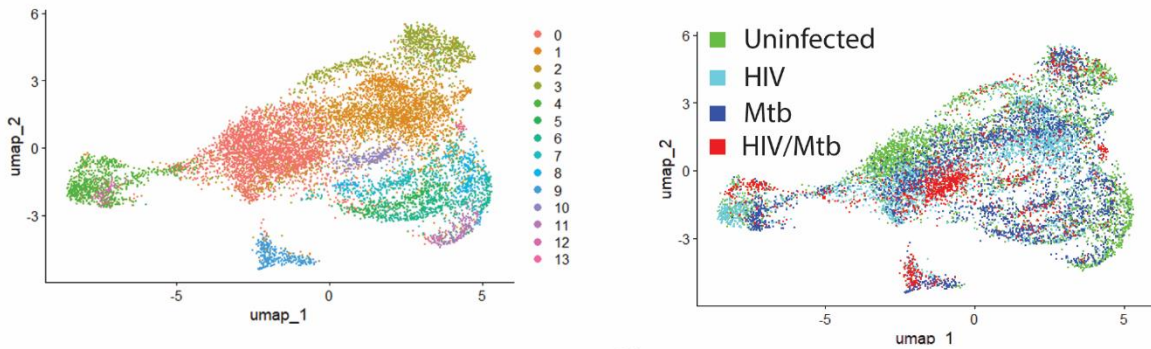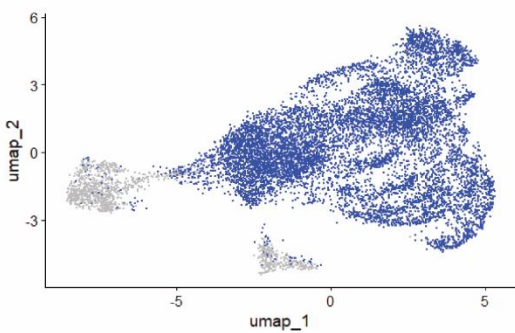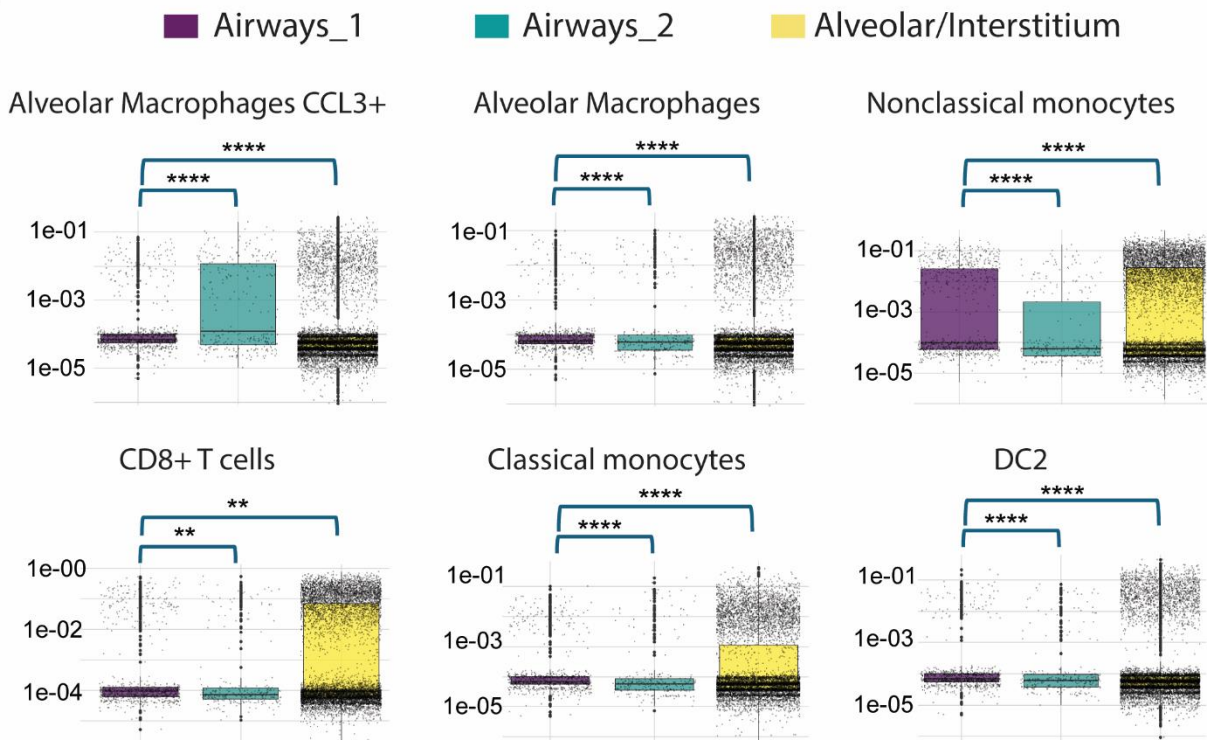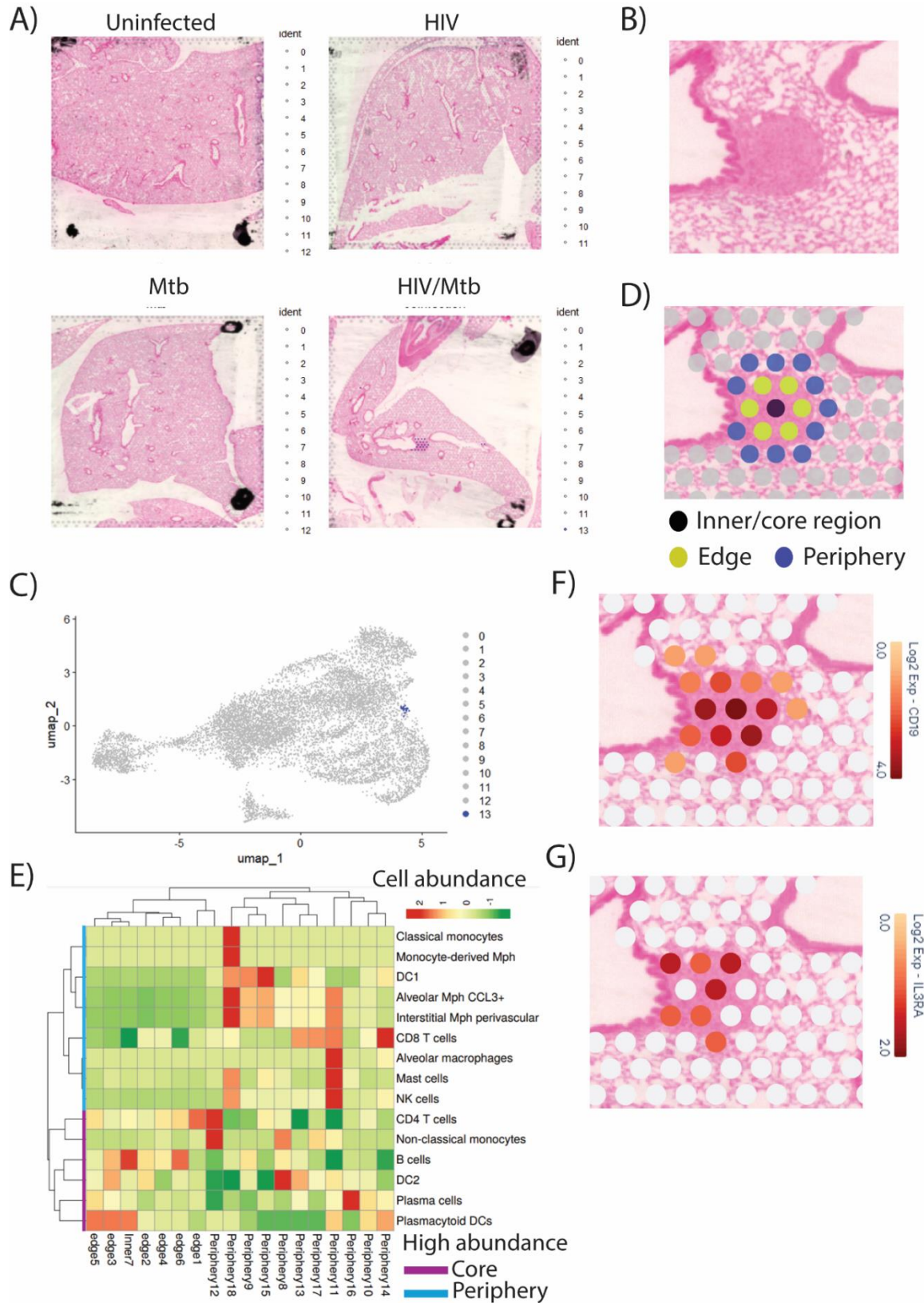
620

621　**Figure 1:**

622

623 **Figure 2:**

624

625 **Figure 3:**

626

627 **Figure 4:**

628